

Connecting Higher-Order Topology with the Orbital Hall Effect in Monolayers of Transition Metal Dichalcogenides

Marcio Costa,^{1,*} Bruno Focassio,^{2,3} Luis M. Canonico,⁴ Tarik P. Cysne,¹ Gabriel R. Schleder,⁵ R. B. Muniz,¹ Adalberto Fazzio,^{2,3} and Tatiana G. Rappoport^{6,7}

¹*Instituto de Física, Universidade Federal Fluminense, 24210-346 Niterói RJ, Brazil*

²*Federal University of ABC (UFABC), 09210-580 Santo André, São Paulo, Brazil*

³*Illum School of Science, CNPEM, 13083-970 Campinas, São Paulo, Brazil*

⁴*Catalan Institute of Nanoscience and Nanotechnology (ICN2), CSIC and BIST, Campus UAB, Bellaterra, 08193 Barcelona, Spain*

⁵*John A. Paulson School of Engineering and Applied Sciences, Harvard University, Cambridge, Massachusetts 02138, USA*

⁶*Instituto de Telecomunicações, Instituto Superior Técnico, University of Lisbon, Avenida Rovisco Pais 1, Lisboa, 1049001 Portugal*

⁷*Instituto de Física, Universidade Federal do Rio de Janeiro, C.P. 68528, 21941-972 Rio de Janeiro RJ, Brazil*

Monolayers of transition metal dichalcogenides (TMDs) in the 2H structural phase have been recently classified as higher-order topological insulators (HOTI), protected by C_3 rotation symmetry. In addition, theoretical calculations show an orbital Hall plateau in the insulating gap of TMDs, characterized by an orbital Chern number. We explore the correlation between these two phenomena in TMD monolayers in two structural phases: the noncentrosymmetric 2H and the centrosymmetric 1T. Using density functional theory, we confirm the characteristics of 2H-TMDs and reveal that 1T-TMDs are identified by a \mathbb{Z}_4 topological invariant. As a result, when cut along appropriate directions, they host conducting edge-states, which cross their bulk energy-band gaps and can transport orbital angular momentum. Our linear response calculations thus indicate that the HOTI phase is accompanied by an orbital Hall effect. Using general symmetry arguments, we establish a connection between the two phenomena with potential implications for orbitronics and spin-orbitronics.

Introduction: The orbital Hall effect (OHE) refers to the transverse flow of orbital angular momentum (OAM) in response to a longitudinally applied electric field. It resembles the spin Hall effect (SHE)¹⁻⁴, but unlike the latter, it does not require spin-orbit coupling (SOC). Characteristics of the OHE and the physical mechanisms underlying it are currently under investigation⁵⁻¹⁰. For instance, signatures of the OHE in 3D metallic systems were recently observed^{11,12}, paving the way for possible orbitronic applications^{1,13,14}.

Lately, the OHE in two-dimensional (2D) materials has received a great deal of attention¹⁵⁻²⁵. Theoretical calculations predict the existence of orbital-textures in some 2D materials, which can give rise to the OHE^{17,18,26,27}. They have been observed in insulating TMDs^{28,29}, where OHE plateaus are predicted¹⁷⁻²⁰. Furthermore, it is possible to attribute an orbital Chern number to this insulating phase^{19,20}, indicating a connection with nontrivial topology.

The topological nature of layered TMDs is mostly focused on the distorted structural phase 1T' that hosts topological insulators³⁰⁻³². Less is known about the topology of octahedral (1T) and trigonal prismatic (2H) structures, where most monolayers exhibit an insulating character³³. MoS₂ is an archetype of a 2H-TMD that exhibits a large energy band gap. Their zigzag nanoribbons display metallic edge-states that cross the bulk gap^{34,35}, suggesting an underlying topology, despite being trivial with respect to the \mathbb{Z}_2 index³⁶.

Refs.^{37,38} have revealed that some 2H-TMDs are 2D higher-order topological insulators (HOTIs), not previously identified by the SHE signature³⁹. Triangular nanoflakes with armchair edges present in-gap corner states with fractional charge, protected by C_3 symmetry. Besides being one of the striking features of a 2D-HOTI³⁹⁻⁴⁴, they explain the presence of metallic edge states in the zigzag edges and connect them to the topology of the 2D material. Their topological bulk polarization is perpendicular to the zigzag edges, leading to charge accumulation and metallic edge states.

Here, we use DFT and linear-response calculations to study the interplay between the OHE and HOTI phases in monolayers of TMDs respecting the rotation symmetry C_3 . We uncover that centrosymmetric 1T-TMDs can also be HOTIs. We then correlate the appearance of a HOTI phase in the two different structures with an orbital Hall insulating phase. We discuss the existence of a pseudo-time reversal symmetry, which originates from the crystalline symmetries of the lattice. In analogy with the photonic quantum spin Hall effect, eigenstates of the orbital angular momentum play the role of pseudo-spins. They are also eigenstates of the C_3 rotation operator that protects the HOTI. Because of the orbital nature of the pseudo-spins, the higher-order topological phase can be witnessed by the OHE. We use a well-known low energy model for HOTIs⁴⁵ and the three d -orbitals model for 2H-TMDs⁴⁶ to explicitly show this connection⁴⁷.

OHE calculations for TMDs in the 2H and 1T struc-

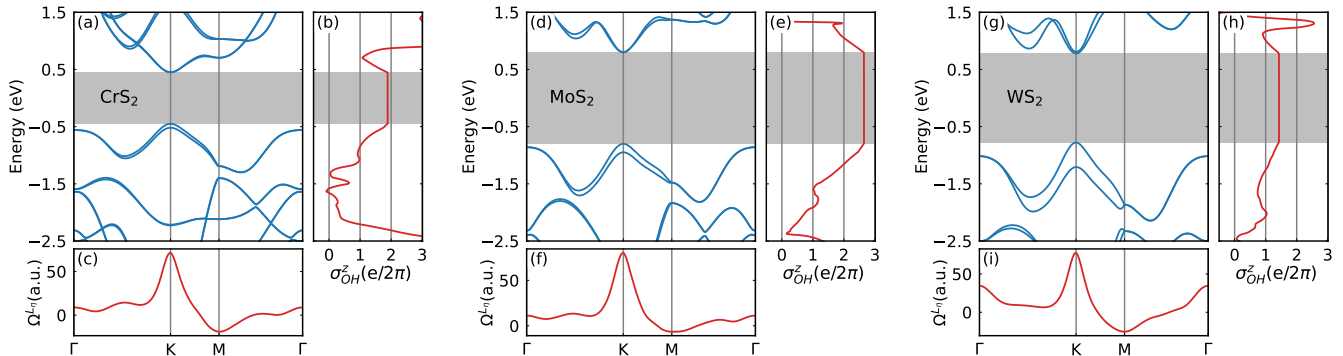


Figure 1: 2H-TMD monolayers of CrS₂, MoS₂ and WS₂ fully relativistic band structures [(a), (d), and (g)] and orbital Berry curvatures [(c), (f), and (i)], calculated along high-symmetry directions of the 2D Brillouin zone. Panels (b), (e), and (h) display the corresponding OH conductivities calculated as function of energy.

tural phases: We begin by presenting the band structure and the OHE for the two families. For that purpose, we performed DFT calculations for 1T and 2H TMD monolayers (MX₂, where M is a transition metal and X is a chalcogen). The TMD structures were obtained from the C2DB database⁴⁸. We also adopted their criteria for dynamic (phonons) and thermodynamic stability. We fully optimize the structural parameters to obtain the wavefunctions. Then, we construct a PAO Hamiltonian using the pseudo-atomic-orbital (PAO) projection method^{49–52} for each compound. This method is implemented in the PAO_{FLOW} code^{53,54}; for technical details see supplementary material (SM).

Once the PAO Hamiltonian $\mathcal{H}_{\text{PAO}}(\mathbf{k})$ is built, we calculate the spin Hall (SH) and orbital Hall (OH) conductivities to linear order on the external electric field^{17–19}

$$\sigma_{OH(SH)}^{\eta} = \frac{e}{(2\pi)^2} \sum_n \int_{\text{BZ}} d^2k f_{n\mathbf{k}} \Omega_{n,\mathbf{k}}^{X_{\eta}}, \quad (1)$$

where $\sigma_{OH(SH)}^{\eta}$ is the OH (SH) DC conductivity with polarization along the η -direction, $f_{n\mathbf{k}}$ is the Fermi-Dirac distribution and $\Omega_{n,\mathbf{k}}^{X_{\eta}}$ is the angular momentum projected Berry curvature in the intra-atomic approximation^{17–19} (see SM⁴⁷).

Figures 1 and 2 show the fully relativistic band structures, OH conductivities and the orbital Berry curvatures calculated for different TMD monolayers. In Fig. 1 we depict results for 2H-TMDs CrS₂, MoS₂ and WS₂. We note that within their insulating gaps these systems exhibit OH conductivity (OHC) plateaus with values $\sigma_{OH}^z = 1.89, 2.65,$ and 1.43 in units of $(\frac{e}{2\pi})$, respectively. Conversely, σ_{OH}^x and σ_{OH}^y vanish for all three systems. Their corresponding orbital Berry curvatures are similar. They are peaked around the K point with similar maxima for the three systems, giving a large positive contribution to the OHC. Around M, the Berry curvature becomes negative and have different values for the three compounds, resulting in the plateau variations ob-

tained for the OHCs when we go from Cr to W. Since the top valence bands of the TMDs have predominantly d -character, the chalcogen element does not significantly affect the OHC. Table 1 of the SM⁴⁷ shows that the in-gap OHC does not change much when S is replaced by Se or Te.

Figure 2 presents results for the 1T-TMDs monolayers NiS₂, PdS₂ and PtS₂. Differently from the 2H-TMDs, the OHCs for the 1T-TMDs with y polarization are not zero, and thus contribute to the entire OHC. We follow ref.⁵⁵ and define the absolute value of the OHC as $|\sigma_{OH}| = \sqrt{(\sigma_{OH}^x)^2 + (\sigma_{OH}^y)^2 + (\sigma_{OH}^z)^2}$. Within each energy band-gap, we clearly see that the dominant contribution to $|\sigma_{OH}|$ is σ_{OH}^z for all three systems, and the OHC plateau reduces as we move from Ni to Pt.

Table I summarizes the main findings depicted in Fig. 2. It is noteworthy that both 2H and 1T TMD monolayers exhibit finite OH conductivity plateaus within their insulating energy gaps. This shows that the OHE in 2D materials is not constrained by spatial inversion symmetry and can also appear in centrosymmetric monolayers. Our results are inline with recent predictions showing that centrosymmetric 2H TMD bilayers also display OHC plateaus^{18–20}. We note that $|\sigma_{SH}| = 0$ inside the band gap for both sets, which is consistent with the fact that TMDs do not exhibit a QSHE in the structural phases studied here. In the SM, we include tables containing several 2H and 1T semiconducting TMD monolayers⁴⁷. We present their electronic band structures and orbital-weighted Berry curvatures for the valence bands and discuss some of their features.

HOTI phase: We now proceed to the characterization of the HOTI phases. Recent works showed that triangular nanoflakes of 2H–TMD monolayers with armchair edges present in-gap corner states with fractional charge $(-\frac{1}{3}|e|)$, protected by C_3 symmetry^{37,38}. We begin our analysis by calculating the topological indicators for this TMD family.

For non-centrosymmetric materials, the HOTI phase is

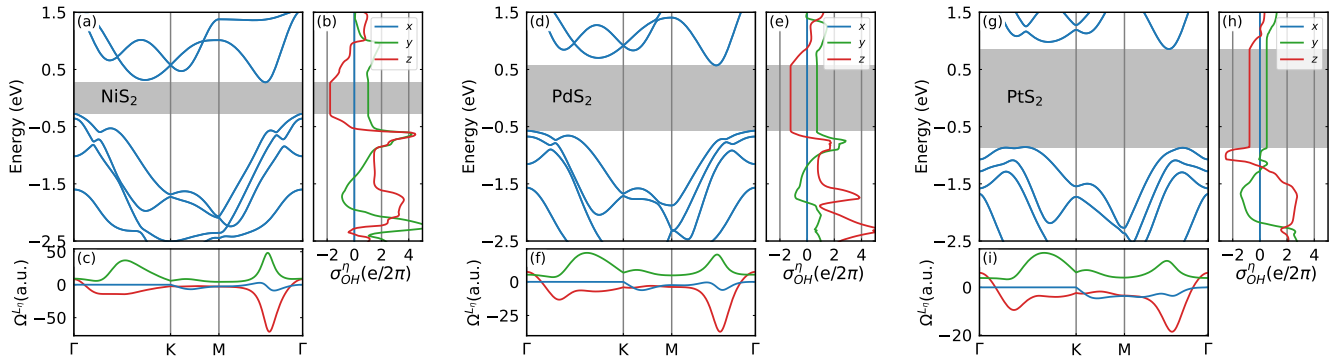


Figure 2: 1T-TMD monolayers of NiS₂, PdS₂ and PtS₂ fully relativistic band structures [(a),(d) and (g)] and orbital Berry curvatures [(c), (f) and (i)], calculated along high-symmetry directions of the 2D Brillouin zone. Panels (b), (e) and (h) display the corresponding OH conductivities calculated as function of energy.

TMD (Z_M)	σ_{OH}^x	σ_{OH}^y	σ_{OH}^z	$ \sigma_{OH} $	E_g (eV)	Z_4
NiS ₂ (28)	0	1.02	-1.78	2.05	0.54	2
PdS ₂ (46)	0	0.73	-1.22	1.85	1.14	2
PtS ₂ (78) ⁵⁶	0	0.51	-0.77	0.92	1.72	2

Table I: Main characteristics of the 1T-TMD monolayers insulating phases of NiS₂, PdS₂, and PtS₂. Z_M is the atomic number of the constituent transition metal atom. The columns σ_{OH}^x , σ_{OH}^y , σ_{OH}^z and $|\sigma_{OH}|$ show their OHE in-gap values in units of $e/(2\pi)$. E_g is the energy band gap and the last column shows the values of the topological invariant Z_4 .

protected by a C_n rotation symmetry. It can be identified by the symmetry representations of the occupied energy bands at special high-symmetry points (HSP) of the first Brillouin zone (BZ)⁴⁴. For C_3 rotation symmetry, we take $[K_p^{(3)}] = \#K_p^{(3)} - \#\Gamma_p^{(3)}$, where $\#K_p^{(3)}$ and $\#\Gamma_p^{(3)}$ represent the number of occupied bands with symmetry eigenvalue $e^{2\pi i(p-1)/3}$ (for $p = 1, 2, 3$) at the K- and Γ -high symmetry points, respectively. The final topological indicator $\chi^{(3)}$ and corner charge $Q_c^{(3)}$ are given by

$$\chi^{(3)} = \left([K_1^{(3)}], [K_2^{(3)}] \right), \quad Q_c^{(3)} = \frac{e}{3} [K_2^{(3)}] \bmod e, \quad (2)$$

where e is the elemental charge. We use the software IrRep⁵⁷ to calculate the symmetry eigenvalues of the occupied DFT energy bands. With them, we calculate the topological indicator and the corner charge with the expressions above. The three 2H-TMD monolayers presented here have the same topological indicator $\chi^{(3)} = [-1, 2]$ and corner charge $Q_c^{(3)} = 2e/3$. A table for several 2H-TMDs is included in the SM⁴⁷.

To complement the analysis based on the eigenstates of the rotation operator, we use DFT to examine 2H-TMD triangular flakes with armchair edges and confirm the presence of in-gap corner states, as shown in figure 3. 2H-TMDs also display an electronic dipole $\mathbf{P} = (\frac{1}{3}, \frac{2}{3})$,

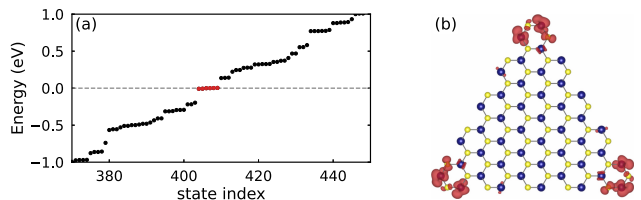


Figure 3: Monolayer MoS₂ nano-flake (0D) geometry. (a) Fully relativistic calculation eigenvalues. The corner states are highlighted in red. (b) Real space projection of the eigenfunctions for the corner states highlighted in panel (a). Iso-surface value of $0.003 \text{ e}\text{\AA}^{-3}$.

which is perpendicular to the zigzag direction³⁷. As a result, if the system is cut in the zigzag direction, there is charge accumulation at the edges, leading to metallic edge states.

Differently from the 2H-TMDs, 1T-TMDs are HOTIs protected by inversion symmetry. Hence, they are characterized by the Z_4 indicator, which can be calculated from the inversion parities of occupied bands^{58,59}: $Z_4 = \sum_{k_i \in \text{TRIMs}} n_-(k_i) \bmod 4$, where $n_-(k_i)$ is the number of odd parity occupied Kramer pairs at the time reversal invariant momenta (TRIM) points k_i in the BZ.

The index $Z_4 = 2$ warrants that 1T-TMDs also present conducting edge-states capable of carrying OAM currents. This can be confirmed from the energy bands of a PtS₂ nanoribbon with zigzag edges portrayed in figure 4. This figure also highlights the orbital projection of the edge states. Because of the inversion symmetry, Bloch states of 1T-TMDs do not exhibit net OAM but can still display OHE³. As a result, the nanoribbon bands do not have any OAM polarization. This contrasts with the 2H-TMD nanoribbons that have well-defined orbital-polarized edge states.

Discussion: We have shown that a large set of insulating 2D materials exhibits sizeable OHE coexisting with a HOTI phase. This shows that higher-order topology

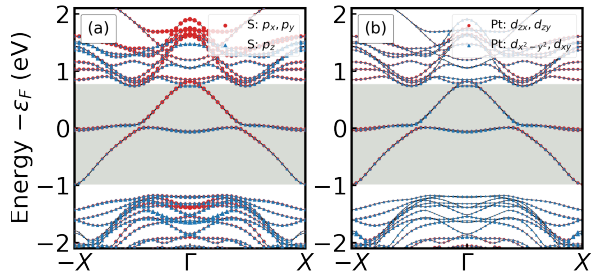


Figure 4: Orbital projected band structures of 18.6 Å-wide zigzag nanoribbon of a PtS₂ monolayer calculated with the PAOFLOW Hamiltonian. The shaded area and colored markers represent the bulk bandgap and orbital projections, respectively. (a) Contributions from the p_x, p_y (red circles) and p_z (blue triangles) orbitals from S atoms. (b) Contributions from the d_{xz}, d_{yz} (red circles) and $d_{x^2-y^2}, d_{xy}$ (blue triangles) orbitals of Pt atoms.

may allow in-gap conducting edge states that can transport orbital angular momentum in the orbital Hall insulating phase. The bulk polarization perpendicular to the edges of a 2D HOTI yields to charge accumulation at the edges. As a result, these systems can have conductive edge states within their bulk energy band gaps when cut along certain directions.

To connect the OHE with the HOTI phase, it is worth recalling how the quantum spin Hall effect (QSHE) is emulated in photonic crystals. For the appearance of a \mathbb{Z}_2 topological phase, one needs Kramers degenerate pairs. However, bosonic systems do not possess half-integer spins. Thus, under the action of time-reversal symmetry operation (\mathcal{T}), they transform as $\mathcal{T}^2 = 1$, whereas for fermionic systems, $\mathcal{T}^2 = -1$ ⁶⁰. To engineer the photonic QSHE, one may construct a Hamiltonian that is invariant under inversion and a pseudo-time-reversal symmetry (\mathcal{T}_p) so that $\mathcal{T}_p^2 = -1$. This is achieved with a lattice of dielectric cylinders, which work as artificial atoms exhibiting electronic orbital-like shapes that produce the photonic bands⁶¹. The pseudo-time-reversal operator originates from a combination of lattice symmetry operations in such a way that the pseudo-spins are eigenstates of L_z such as $p_{\pm} = p_x \pm ip_y$ and $d_{\pm} = d_{xy} \pm id_{x^2-y^2}$ ^{61,62}.

To identify these pseudo-spins in the TMDs, we can use general symmetry considerations regarding 2D materials with 3-fold rotational symmetry. The crystal field in low-dimensional systems leads to large splittings between orbitals, inducing the formation of energy gaps. However, the rotational symmetry also imposes constraints on the energy states. These have to be also eigenstates of the rotation operator at the high symmetry points.

For 2H-TMDs, the conduction and valence bands at K and K' are mainly composed of d_{z^2} and d_{\pm} orbitals, which are eigenstates of L_z . This is a consequence of the D_{3h} point group symmetry of the crystal: the d_{z^2} orbitals belong to the unidimensional irreducible representation

A_1 , while the d_{xy} and $d_{x^2-y^2}$ belong to E' . Since the representation E' is 2-dimensional, the linear combinations d_{\pm} can be treated as pseudo-spins that transform under a pseudo-time-reversal symmetry operator related to the rotation operators. In the SM⁴⁷, we show that the Chern number associated with \mathcal{T}_p symmetry leads to the same result previously obtained¹⁹.

In the case of the 1T TMDs, the identification of the pseudo-spins is more subtle. The D_{3d} symmetry imposes that the p orbitals of the X atoms and the d orbitals from the M atom should be dominant for the bulk energy states near Γ . Our first-principles calculations⁴⁷ evince a strong energy splitting in Γ between the p_x, p_y and the p_z orbitals, as previously reported by Yao *et al.* for PtSe₂⁶³. The valence and conduction bands near the gap have a strong contribution of linear combinations of p_x and p_y orbitals of the X atom that form p_{\pm} , which transform as $\mathcal{T}_p^2 = -1$. They are also composed of d_{\pm} . The sizable contribution of d_{xz} and d_{yz} orbitals explain L_x and L_y components of the OHE. When the system is cut into a ribbon, these orbitals participate in the formation of edge states, as shown in Fig. 4(b). Therefore, in contrast with 2H-TMDs, these edge states will be mainly composed of combinations of three pseudo-spins, one formed by the p_x, p_y orbitals and two composed of the $d_{xz}, d_{yz}, d_{x^2-y^2}$, and d_{xy} orbitals.

In principle, similar to photonics systems, one could use these eigenstates of L_z to emulate topological phases in fermionic materials: a system which is invariant under inversion and \mathcal{T}_p , must have pseudo-spins forming Kramers' pairs. However, differently from bosons, fermions have half-integer spins, and two spin-degenerate states for each pseudo-spin. Therefore, if one tries to construct a fermionic system without spin-orbit coupling where the pseudo-spins emulate a quantum spin Hall insulator, the system has spin-degenerate pseudo-spins Kramers' pairs. This results in an even number of Kramers' pairs and the system cannot be indexed by a $\mathbb{Z}_2 = 1$, although it can be a HOTI.

To illustrate these ideas, we use the low energy Hamiltonian presented in Ref. 45 to model HOTIs protected by C_3 rotation and inversion symmetries (see SM⁴⁷). This model consists of a block diagonal Hamiltonian containing basically the superposition of two copies of the Bernevig-Hughes-Zhang (BHZ) model. It is well known that each BHZ Hamiltonian presents a \mathbb{Z}_2 topological phase. Its eigenstates can also be written in terms of pseudo-spins that are eigenstates of L_z . Surprisingly, we show they present an orbital Hall plateau in their topological gap. When the two BHZ copies are taken into account, the system is not a topological insulator but, as shown in Ref. 45, it is a HOTI that has twice the number of edge states of the BHZ model. As expected, the HOTI still presents an orbital Hall plateau and the orbital current can be carried by the in-gap edge states.

To strengthen this link, we used another model to show the onset of a HOTI phase in systems without inversion symmetry, following the ideas presented in Ref. 64.

We considered the simplified three orbital tight-binding Hamiltonian in a triangular lattice that describes the low-energy properties of 2H-TMDs. We begin with a case with inversion symmetry and orthogonality between the orbitals in different representations. Under this condition, a strong spin-orbit coupling opens a gap in the system, leading to a trivial insulator phase with a vanishing OHE and the absence of in-gap edge states. From this, we identify that if inversion symmetry is broken and hopping between orthogonal orbitals is allowed, as in the case of 2H-TMD, there is a topological transition to a HOTI that presents zigzag metallic edge states and a large OH plateau, which is independent of the SOC⁴⁷.

Conclusions: We employed DFT and linear response transport calculations to study the interplay between the orbital Hall effect and higher-order topological phases. We analyzed all stable 2H or 1T monolayer TMDs and found that they are HOTIs, protected by either C_3 rotation symmetry (2H) or inversion symmetry (1T). Simultaneously, they all display a plateau in the orbital Hall conductivity inside the band gap.

Recent works start to uncover the role of orbital hybridization in HOTIs and the advent of orbital effects^{64–66}. Here, we connect the HOTI phase to the existence of pseudo-time reversal operators and associated pseudo-spinors. As these pseudo-spinors are eigenstates of the orbital angular momentum, HOTI phases can generate OHE. More importantly, HOTIs with edges that are perpendicular to their bulk polarization present in-gap metallic edge states that can carry the orbital angular momentum in the orbital Hall insulating phase. This can be employed for efficient orbital current injection in novel spin-orbitronics devices. Furthermore, the OHE in

2D HOTIs may be used in machine learning strategies for spotting potentially useful materials for orbitronic applications^{67–69}.

Acknowledgments

We acknowledge CNPq/Brazil, CAPES/Brazil, FAPERJ/Brazil, INCT Nanocarbono and INCT Materials Informatics for financial support. TGR acknowledges funding from Fundação para a Ciência e a Tecnologia and Instituto de Telecomunicações - grant number UID/50008/2020 in the framework of the project Sym-Break. M. C. acknowledges CNPq (Grant No. 317320/2021-1) FAPERJ/Brazil (Grant No. E26/200.240/2023) and the National Laboratory for Scientific Computing (LNCC/MCTI, Brazil) for providing HPC resources. B.F. acknowledges funding from FAPESP/Brazil under grant no. 2019/04527-0 and the Brazilian Nanotechnology National Laboratory (LNNano/CNPEM, Brazil) for computational resources. A.F. acknowledges funding from FAPESP/Brazil under grant no. 2017/02317-2. L.M.C acknowledges the funding from the ECONWHET project, reference PID2019-106684GB-I00, funded by MCIN/AEI/10.13039/501100011033/ and by "ERDF A way of making Europe". ICN2 is funded by the CERCA Programme/Generalitat de Catalunya and supported by the Severo Ochoa Centres of Excellence program, funded by the Spanish Research Agency (Grant No. SEV-2017-0706).

* Electronic address: mjtcosta@id.uff.br

¹ D. Go, D. Jo, H.-W. Lee, M. Kläui, and Y. Mokrousov, EPL (Europhysics Letters) **135**, 37001 (2021), URL <https://doi.org/10.1209/2F0295-5075%2Fac2653>.

² B. A. Bernevig, T. L. Hughes, and S.-C. Zhang, Phys. Rev. Lett. **95**, 066601 (2005), URL <https://link.aps.org/doi/10.1103/PhysRevLett.95.066601>.

³ D. Go, D. Jo, C. Kim, and H.-W. Lee, Phys. Rev. Lett. **121**, 086602 (2018), URL <https://link.aps.org/doi/10.1103/PhysRevLett.121.086602>.

⁴ D. Jo, D. Go, and H.-W. Lee, Phys. Rev. B **98**, 214405 (2018), URL <https://link.aps.org/doi/10.1103/PhysRevB.98.214405>.

⁵ L. Salemi and P. M. Oppeneer, *First-principles theory of intrinsic spin and orbital hall and nernst effects in metallic monoatomic crystals* (2022), URL <https://arxiv.org/abs/2203.17037>.

⁶ L. Salemi and P. M. Oppeneer, *Theory of magnetic spin and orbital hall and nernst effects in bulk ferromagnets* (2022), URL <https://arxiv.org/abs/2203.17025>.

⁷ L. Salemi, M. Berritta, and P. M. Oppeneer, Phys. Rev. Materials **5**, 074407 (2021), URL <https://link.aps.org/doi/10.1103/PhysRevMaterials.5.074407>.

⁸ P. Sahu, S. Bhowal, and S. Satpathy, Phys. Rev. B **103**, 085113 (2021), URL <https://link.aps.org/doi/10.1103/PhysRevB.103.085113>.

⁹ I. Baek and H.-W. Lee, Phys. Rev. B **104**, 245204 (2021), URL <https://link.aps.org/doi/10.1103/PhysRevB.104.245204>.

¹⁰ H. Lee, B. Choi, and H.-W. Lee, Phys. Rev. B **105**, 035142 (2022), URL <https://link.aps.org/doi/10.1103/PhysRevB.105.035142>.

¹¹ Y.-G. Choi, D. Jo, K.-H. Ko, D. Go, K.-H. Kim, H. G. Park, C. Kim, B.-C. Min, G.-M. Choi, and H.-W. Lee, *Observation of the orbital hall effect in a light metal ti* (2021), URL <https://arxiv.org/abs/2109.14847>.

¹² D. Lee, D. Go, H.-J. Park, W. Jeong, H.-W. Ko, D. Yun, D. Jo, S. Lee, G. Go, J. H. Oh, et al., Nature Communications **12**, 6710 (2021), URL <https://doi.org/10.1038/s41467-021-26650-9>.

¹³ S. Park and B.-J. Yang, Nano Letters **20**, 7694 (2020), URL <https://doi.org/10.1021/acs.nanolett.0c03220>.

¹⁴ D. Go, D. Jo, T. Gao, K. Ando, S. Blügel, H.-W. Lee, and Y. Mokrousov, Phys. Rev. B **103**, L121113 (2021), URL <https://link.aps.org/doi/10.1103/PhysRevB.103.L121113>.

- ¹⁵ F. Xue, V. Amin, and P. M. Haney, *Phys. Rev. B* **102**, 161103 (2020), URL <https://link.aps.org/doi/10.1103/PhysRevB.102.161103>.
- ¹⁶ T. P. Cysne, F. S. M. Guimarães, L. M. Canonico, T. G. Rappoport, and R. B. Muniz, *Phys. Rev. B* **104**, 165403 (2021), URL <https://link.aps.org/doi/10.1103/PhysRevB.104.165403>.
- ¹⁷ L. M. Canonico, T. P. Cysne, T. G. Rappoport, and R. B. Muniz, *Phys. Rev. B* **101**, 075429 (2020), URL <https://link.aps.org/doi/10.1103/PhysRevB.101.075429>.
- ¹⁸ L. M. Canonico, T. P. Cysne, A. Molina-Sanchez, R. B. Muniz, and T. G. Rappoport, *Phys. Rev. B* **101**, 161409 (2020), URL <https://link.aps.org/doi/10.1103/PhysRevB.101.161409>.
- ¹⁹ T. P. Cysne, M. Costa, L. M. Canonico, M. B. Nardelli, R. B. Muniz, and T. G. Rappoport, *Phys. Rev. Lett.* **126**, 056601 (2021), URL <https://link.aps.org/doi/10.1103/PhysRevLett.126.056601>.
- ²⁰ T. P. Cysne, S. Bhowal, G. Vignale, and T. G. Rappoport, *Phys. Rev. B* **105**, 195421 (2022), URL <https://link.aps.org/doi/10.1103/PhysRevB.105.195421>.
- ²¹ V. o. T. Phong, Z. Addison, S. Ahn, H. Min, R. Agarwal, and E. J. Mele, *Phys. Rev. Lett.* **123**, 236403 (2019), URL <https://link.aps.org/doi/10.1103/PhysRevLett.123.236403>.
- ²² S. Bhowal and S. Satpathy, *Phys. Rev. B* **102**, 035409 (2020), URL <https://link.aps.org/doi/10.1103/PhysRevB.102.035409>.
- ²³ S. Bhowal and G. Vignale, *Phys. Rev. B* **103**, 195309 (2021), URL <https://link.aps.org/doi/10.1103/PhysRevB.103.195309>.
- ²⁴ X. Mu, Y. Pan, and J. Zhou, *npj Comput Mater* **7**, 61 (2021), URL <https://doi.org/10.1038/s41524-021-00531-7>.
- ²⁵ Y. Shi and J. Zhou, *Phys. Rev. B* **104**, 155146 (2021), URL <https://link.aps.org/doi/10.1103/PhysRevB.104.155146>.
- ²⁶ F. C. de Lima, G. J. Ferreira, and R. H. Miwa, *Nano Letters* **19**, 6564 (2019), URL <https://doi.org/10.1021/acs.nanolett.9b02802>.
- ²⁷ L. M. Canonico, T. G. Rappoport, and R. B. Muniz, *Phys. Rev. Lett.* **122**, 196601 (2019), URL <https://link.aps.org/doi/10.1103/PhysRevLett.122.196601>.
- ²⁸ S. Beaulieu, J. Schusser, S. Dong, M. Schüler, T. Pincelli, M. Dendzik, J. Maklar, A. Neef, H. Ebert, K. Hricovini, et al., *Phys. Rev. Lett.* **125**, 216404 (2020), URL <https://link.aps.org/doi/10.1103/PhysRevLett.125.216404>.
- ²⁹ S. Beaulieu, M. Schüler, J. Schusser, S. Dong, T. Pincelli, J. Maklar, A. Neef, F. Reinert, M. Wolf, L. Rettig, et al., *npj Quantum Materials* **6**, 93 (2021), URL <https://doi.org/10.1038/s41535-021-00398-3>.
- ³⁰ X. Qian, J. Liu, L. Fu, and J. Li, *Science* **346**, 1344 (2014), URL <https://doi.org/10.1126/science.1256815>.
- ³¹ S. Tang, C. Zhang, D. Wong, Z. Pedramrazi, H.-Z. Tsai, C. Jia, B. Moritz, M. Claassen, H. Ryu, S. Kahn, et al., *Nature Physics* **13**, 683 (2017), URL <https://doi.org/10.1038/nphys4174>.
- ³² F. Giustino, J. H. Lee, F. Trier, M. Bibes, S. M. Winter, R. Valentí, Y.-W. Son, L. Taillefer, C. Heil, A. I. Figueroa, et al., *Journal of Physics: Materials* **3**, 042006 (2020), URL <https://doi.org/10.1088/2515-7639/abb74e>.
- ³³ S. Manzeli, D. Ovchinnikov, D. Pasquier, O. V. Yazyev, and A. Kis, *Nature Reviews Materials* **2**, 17033 (2017), URL <https://doi.org/10.1038/natrevmats.2017.33>.
- ³⁴ E. Ridolfi, L. R. F. Lima, E. R. Mucciolo, and C. H. Lewenkopf, *Phys. Rev. B* **95**, 035430 (2017), URL <https://link.aps.org/doi/10.1103/PhysRevB.95.035430>.
- ³⁵ H. Rostami, R. Asgari, and F. Guinea, *Journal of Physics: Condensed Matter* **28**, 495001 (2016), URL <https://doi.org/10.1088/2F0953-8984/2F28/2F49/2F495001>.
- ³⁶ T. Frank, P. Högl, M. Gmitra, D. Kochan, and J. Fabian, *Phys. Rev. Lett.* **120**, 156402 (2018), URL <https://link.aps.org/doi/10.1103/PhysRevLett.120.156402>.
- ³⁷ J. Zeng, H. Liu, H. Jiang, Q.-F. Sun, and X. C. Xie, *Phys. Rev. B* **104**, L161108 (2021), URL <https://link.aps.org/doi/10.1103/PhysRevB.104.L161108>.
- ³⁸ S. Qian, G.-B. Liu, C.-C. Liu, and Y. Yao, *Phys. Rev. B* **105**, 045417 (2022), URL <https://link.aps.org/doi/10.1103/PhysRevB.105.045417>.
- ³⁹ M. Costa, G. R. Schleder, C. M. Acosta, A. C. M. Padilha, F. Cerasoli, M. B. Nardelli, and A. Fazzio, *npj Computational Materials* **7**, 49 (2021), URL <https://doi.org/10.1038/s41524-021-00518-4>.
- ⁴⁰ R.-J. Slager, L. Rademaker, J. Zaanen, and L. Balents, *Phys. Rev. B* **92**, 085126 (2015), URL <https://link.aps.org/doi/10.1103/PhysRevB.92.085126>.
- ⁴¹ W. A. Benalcazar, B. A. Bernevig, and T. L. Hughes, *Science* **357**, 61 (2017), URL <https://doi.org/10.1126/science.aah6442>.
- ⁴² W. A. Benalcazar, B. A. Bernevig, and T. L. Hughes, *Phys. Rev. B* **96**, 245115 (2017), URL <https://link.aps.org/doi/10.1103/PhysRevB.96.245115>.
- ⁴³ Z. Song, Z. Fang, and C. Fang, *Phys. Rev. Lett.* **119**, 246402 (2017), URL <https://link.aps.org/doi/10.1103/PhysRevLett.119.246402>.
- ⁴⁴ W. A. Benalcazar, T. Li, and T. L. Hughes, *Phys. Rev. B* **99**, 245151 (2019), URL <https://link.aps.org/doi/10.1103/PhysRevB.99.245151>.
- ⁴⁵ F. Schindler, Z. Wang, M. G. Vergniory, A. M. Cook, A. Murani, S. Sengupta, A. Y. Kasumov, R. Deblock, S. Jeon, I. Drozdov, et al., *Nature Physics* **14**, 918 (2018), URL <https://doi.org/10.1038/s41567-018-0224-7>.
- ⁴⁶ G.-B. Liu, W.-Y. Shan, Y. Yao, W. Yao, and D. Xiao, *Physical Review B* **88**, 085433 (2013).
- ⁴⁷ Supplementary Material containing tables and figures for another 11 2H and 12 1T TMD monolayers, , URL [XXX](#).
- ⁴⁸ S. Hastrup, M. Strange, M. Pandey, T. Deilmann, P. S. Schmidt, N. F. Hinsche, M. N. Gjerding, D. Torelli, P. M. Larsen, A. C. Riis-Jensen, et al., *2D Materials* **5**, 042002 (2018), URL <https://doi.org/10.1088/2053-1583/aacfc1>.
- ⁴⁹ L. A. Agapito, A. Ferretti, A. Calzolari, S. Curtarolo, and M. Buongiorno Nardelli, *Phys. Rev. B* **88**, 165127 (2013), URL <https://link.aps.org/doi/10.1103/PhysRevB.88.165127>.
- ⁵⁰ L. A. Agapito, S. Curtarolo, and M. Buongiorno Nardelli, *Phys. Rev. X* **5**, 011006 (2015), URL <https://link.aps.org/doi/10.1103/PhysRevX.5.011006>.
- ⁵¹ L. A. Agapito, M. Fornari, D. Ceresoli, A. Ferretti, S. Curtarolo, and M. Buongiorno Nardelli, *Phys. Rev. B* **93**, 125137 (2016), URL <https://link.aps.org/doi/10.1103/PhysRevB.93.125137>.
- ⁵² L. A. Agapito, S. Ismail-Beigi, S. Curtarolo, M. Fornari, and M. Buongiorno Nardelli, *Phys. Rev. B* **93**, 035104 (2016), URL <https://link.aps.org/doi/10.1103/PhysRevB.93.035104>.
- ⁵³ M. Buongiorno Nardelli, F. T. Cerasoli, M. Costa, S. Curtarolo, R. D. Gennaro, M. Fornari, L. Liyan-

- age, A. R. Supka, and H. Wang, *Computational Materials Science* **143**, 462 (2018), ISSN 0927-0256, URL <http://www.sciencedirect.com/science/article/pii/S0927025617306651>.
- ⁵⁴ F. T. Cerasoli, A. R. Supka, A. Jayaraj, M. Costa, I. Siloi, J. Sławińska, S. Curtarolo, M. Fornari, D. Ceresoli, and M. Buongiorno Nardelli, *Computational Materials Science* **200**, 110828 (2021), ISSN 0927-0256, URL <https://www.sciencedirect.com/science/article/pii/S0927025621005486>.
- ⁵⁵ J. H. Garcia, M. Vila, C.-H. Hsu, X. Waintal, V. M. Pereira, and S. Roche, *Phys. Rev. Lett.* **125**, 256603 (2020), URL <https://link.aps.org/doi/10.1103/PhysRevLett.125.256603>.
- ⁵⁶ Y. Zhao, J. Qiao, P. Yu, Z. Hu, Z. Lin, S. P. Lau, Z. Liu, W. Ji, and Y. Chai, *Advanced Materials* **28**, 2399 (2016), URL <https://doi.org/10.1002/adma.201504572>.
- ⁵⁷ M. Iraola, J. L. Mañes, B. Bradlyn, M. K. Horton, T. Neupert, M. G. Vergniory, and S. S. Tsirkin, *Computer Physics Communications* **272**, 108226 (2022), ISSN 0010-4655, URL <https://www.sciencedirect.com/science/article/pii/S0010465521003386>.
- ⁵⁸ J. Kruthoff, J. de Boer, J. van Wezel, C. L. Kane, and R.-J. Slager, *Phys. Rev. X* **7**, 041069 (2017), URL <https://link.aps.org/doi/10.1103/PhysRevX.7.041069>.
- ⁵⁹ E. Khalaf, H. C. Po, A. Vishwanath, and H. Watanabe, *Phys. Rev. X* **8**, 031070 (2018), URL <https://link.aps.org/doi/10.1103/PhysRevX.8.031070>.
- ⁶⁰ T. Ozawa, H. M. Price, A. Amo, N. Goldman, M. Hafezi, L. Lu, M. C. Rechtsman, D. Schuster, J. Simon, O. Zeitlinger, et al., *Rev. Mod. Phys.* **91**, 015006 (2019), URL <https://link.aps.org/doi/10.1103/RevModPhys.91.015006>.
- ⁶¹ L.-H. Wu and X. Hu, *Phys. Rev. Lett.* **114**, 223901 (2015), URL <https://link.aps.org/doi/10.1103/PhysRevLett.114.223901>.
- ⁶² J. Mei, Z. Chen, and Y. Wu, *Scientific Reports* **6**, 32752 (2016), URL <https://doi.org/10.1038/srep32752>.
- ⁶³ W. Yao, E. Wang, H. Huang, K. Deng, M. Yan, K. Zhang, K. Miyamoto, T. Okuda, L. Li, Y. Wang, et al., *Nature Communications* **8**, 14216 (2017), URL <https://doi.org/10.1038/ncomms14216>.
- ⁶⁴ P. Eck, Y. Fang, D. Di Sante, G. Sangiovanni, and J. Cano, *Recipe for higher-order topology on the triangular lattice* (2022), URL <https://arxiv.org/abs/2207.01359>.
- ⁶⁵ M. Mazanov and M. A. Gorlach, *Phys. Rev. B* **105**, 205117 (2022), URL <https://link.aps.org/doi/10.1103/PhysRevB.105.205117>.
- ⁶⁶ J. Gliozzi, M. Lin, and T. L. Hughes, *Orbital magnetic quadrupole moment in higher order topological phases* (2022), URL <https://arxiv.org/abs/2211.08438>.
- ⁶⁷ G. R. Schleder, B. Focassio, and A. Fazzio, *Applied Physics Reviews* **8**, 031409 (2021), URL <https://doi.org/10.1063/5.0055035>.
- ⁶⁸ G. R. Schleder, C. M. Acosta, and A. Fazzio, *ACS Applied Materials & Interfaces* **12**, 20149 (2019), URL <https://doi.org/10.1021/acsami.9b14530>.
- ⁶⁹ G. R. Schleder, A. C. M. Padilha, A. R. Rocha, G. M. Dalpian, and A. Fazzio, *Journal of Chemical Information and Modeling* **60**, 452 (2019), URL <https://doi.org/10.1021/acs.jcim.9b00781>.
- ⁷⁰ P. Hohenberg and W. Kohn, *Phys. Rev.* **136**, B864 (1964), URL <https://link.aps.org/doi/10.1103/PhysRev.136.B864>.
- ⁷¹ W. Kohn and L. J. Sham, *Phys. Rev.* **140**, A1133 (1965), URL <https://link.aps.org/doi/10.1103/PhysRev.140.A1133>.
- ⁷² P. Giannozzi, O. Andreussi, T. Brumme, O. Bunau, M. Buongiorno Nardelli, M. Calandra, R. Car, C. Cavazzoni, D. Ceresoli, M. Cococcioni, et al., *Journal of Physics: Condensed Matter* **29**, 465901 (2017), URL <http://stacks.iop.org/0953-8984/29/i=46/a=465901>.
- ⁷³ J. P. Perdew, K. Burke, and M. Ernzerhof, *Phys. Rev. Lett.* **77**, 3865 (1996), URL <https://link.aps.org/doi/10.1103/PhysRevLett.77.3865>.
- ⁷⁴ G. Kresse and D. Joubert, *Phys. Rev. B* **59**, 1758 (1999), URL <https://link.aps.org/doi/10.1103/PhysRevB.59.1758>.
- ⁷⁵ A. Dal Corso, *Computational Materials Science* **95**, 337 (2014), ISSN 0927-0256, URL <https://www.sciencedirect.com/science/article/pii/S0927025614005187>.
- ⁷⁶ M. Costa, G. R. Schleder, M. Buongiorno Nardelli, C. Lewenkopf, and A. Fazzio, *Nano Letters* **19**, 8941 (2019), URL <https://doi.org/10.1021/acs.nanolett.9b03881>.
- ⁷⁷ M. Costa, A. T. Costa, W. A. Freitas, T. M. Schmidt, M. Buongiorno Nardelli, and A. Fazzio, *ACS Omega* **3**, 15900 (2018), URL <https://doi.org/10.1021/acsomega.8b01836>.
- ⁷⁸ M. Costa, M. B. Nardelli, A. Fazzio, and A. T. Costa, *Long range dynamical coupling between magnetic adatoms mediated by a 2d topological insulator* (2018), URL <https://arxiv.org/abs/1808.00347>.
- ⁷⁹ M. Costa, N. M. R. Peres, J. Fernández-Rossier, and A. T. Costa, *Phys. Rev. B* **102**, 014450 (2020), URL <https://link.aps.org/doi/10.1103/PhysRevB.102.014450>.
- ⁸⁰ J. J. Heath, M. Costa, M. Buongiorno-Nardelli, and M. A. Kuroda, *Phys. Rev. B* **101**, 195439 (2020), URL <https://link.aps.org/doi/10.1103/PhysRevB.101.195439>.
- ⁸¹ L. Fu and C. L. Kane, *Phys. Rev. B* **76**, 045302 (2007), URL <https://link.aps.org/doi/10.1103/PhysRevB.76.045302>.
- ⁸² J. Mei, Z. Chen, and Y. Wu, *Scientific reports* **6**, 1 (2016).

Supplementary material for “Connecting Higher-Order Topology with the Orbital Hall Effect in Monolayers of Transition Metal Dichalcogenides”

I. CALCULATION OF THE ORBITAL HALL CONDUCTIVITY: COMPUTATIONAL DETAILS

The density functional theory (DFT) calculations^{70,71} were performed with the plane-wave-based code QUANTUM ESPRESSO⁷². The exchange and correlation potential were treated within the generalized gradient approximation (GGA)⁷³. The ionic cores were described with fully relativistic projected augmented wave (PAW) potentials⁷⁴. The wavefunctions and charge density energy were 40% larger than the pslibrary recommended⁷⁵ value. Our self-consistent calculations (SCF) were performed with a linear density of \mathbf{k} -points of $12.0/\text{\AA}^{-1}$, and to avoid spurious interactions a minimum of 15\AA of vacuum is used.

We constructed an effective tight-binding Hamiltonian from our DFT calculations using the pseudo atomic orbital projection (PAO) method^{49,51} as implemented in the PAOWFLOW code^{53,54}. The PAO method consists of projecting the several thousand plane-waves DFT Kohn-Sham orbitals onto the compact subspace spanned by the pseudo atomic orbitals, which are naturally built-in into the PAW potentials. This procedure significantly reduces the computational cost of performing large integration's. We have used this method to investigate topological properties^{76,77}, spin dynamics^{78,79}, transport properties^{39,80} and others. The orbital Hall conductivity calculations were performed with a reciprocal space sampling 10 times larger than the DFT-SCF calculations.

II. ORBITAL WEIGHTED BERRY CURVATURE AND ELECTRONIC SPECTRA

The orbital-weighted Berry curvature $\Omega_{n,\mathbf{k}}^{X_\eta}$ is given by

$$\Omega_{n,\mathbf{k}}^{X_\eta} = 2\hbar \sum_{m \neq n} \text{Im} \left[\frac{\langle u_{n,\mathbf{k}} | j_{y,\mathbf{k}}^{X_\eta} | u_{m,\mathbf{k}} \rangle \langle u_{m,\mathbf{k}} | v_x(\mathbf{k}) | u_{n,\mathbf{k}} \rangle}{(E_{n,\mathbf{k}} - E_{m,\mathbf{k}} + i0^+)^2} \right]. \quad (\text{S3})$$

The velocity operators are given by $v_{x(y)}(\mathbf{k}) = \hbar^{-1} \partial \mathcal{H}_{\text{PAO}}(\mathbf{k}) / \partial k_{x(y)}$, and $|u_{n(m),\mathbf{k}}\rangle$ is the periodic part of Bloch wave function with energy $E_{n(m),\mathbf{k}}$. The orbital (spin) current polarized in η -direction ($\eta = x, y, z$) is defined by $j_{y,\mathbf{k}}^{X_\eta} = (X_\eta v_y(\mathbf{k}) + v_y(\mathbf{k}) X_\eta) / 2$, where $X_\eta = \hat{\ell}_\eta(\hat{s}_\eta)$ is the η -component of OAM (spin) operator. Here, we use the intra-atomic approximation for the OAM operator that gives a reliable description of the OHE for TMDs^{19,20}.

The orbital-weighted Berry curvature of the valence-band is defined as the sum over the occupied valence-band states of the individual orbital-weighted curvatures given by

$$\Omega^{L_\eta}(\mathbf{k}) = \sum_{n \in \text{val}} \Omega_{n,\mathbf{k}}^{L_\eta}. \quad (\text{S4})$$

At zero temperature and for Fermi energies within the TMD band gap, we note that the orbital-Hall-conductivity plateau σ_{OH}^η , associated to orbital angular momentum component L_η ($\eta = x, y, z$), is given by

$$\sigma_{OH}^\eta = \frac{e}{(2\pi)^2} \int_{\text{BZ}} d^2k \Omega^{L_\eta}(\mathbf{k}), \quad (\text{S5})$$

where the integral is over the Brillouin zone (BZ). Here, we follow Ref. 55 and define $|\sigma_{OH}| = \sqrt{(\sigma_{OH}^x)^2 + (\sigma_{OH}^y)^2 + (\sigma_{OH}^z)^2}$.

In the following sections we present our DFT-calculated results of σ_{OH}^η and $|\sigma_{OH}|$ for several TMD monolayers in the 2H and 1T structural phases, together with their corresponding electronic energy bands.

III. 2H-TMDS

Table II extends the table I presented in the main text. It includes all insulating TMD monolayers that naturally stabilize in the 2H structural phase. They are listed here in decreasing order of their orbital Hall conductivity plateaus.

H-TMD (Z_M)	σ_{OH}^x	σ_{OH}^y	σ_{OH}^z	$ \sigma_{OH} $	$ \sigma_{SH} $	E_g (eV)	$K_1^{(3)}$	$K_2^{(3)}$	$Q_c^{(3)}$
MoS ₂ (42)	0.00	0.00	2.65	2.65	0.00	1.60	-1	2	2/3
MoSe ₂ (42)	0.00	0.00	2.63	2.63	0.00	1.34	-1	2	2/3
MoTe ₂ (42)	0.00	0.00	2.47	2.47	0.00	0.95	-1	2	2/3
CrS ₂ (24)	0.00	0.00	1.89	1.89	0.00	0.90	-1	2	2/3
CrSe ₂ (24)	0.00	0.00	1.92	1.92	0.00	0.71	-1	2	2/3
CrTe ₂ (24)	0.00	0.00	1.91	1.91	0.00	0.47	-1	2	2/3
WS ₂ (74)	0.00	0.00	1.43	1.43	0.00	1.56	-1	2	2/3
WSe ₂ (74)	0.00	0.00	1.63	1.63	0.00	1.27	-1	2	2/3
WTe ₂ (74)	0.00	0.00	1.46	1.46	0.00	0.77	-1	2	2/3
TiS ₂ (22)	0.00	0.00	0.78	0.78	0.00	0.72	0	2	2/3
TiSe ₂ (22)	0.00	0.00	0.75	0.75	0.00	0.53	0	2	2/3

Table II: Orbital Hall conductivity of TMD monolayers in the 2H structural phase. In the first column, we list the compound and the atomic number of its transition metal atom (Z_M). Columns 2-5 show the corresponding OHCs inside their insulating gaps (σ_{OH}^η , for $\eta = x, y, z$, and $|\sigma_{OH}|$), respectively. All the OHCs are given in units of $e/2\pi$. We note that inside their gaps all the 2H TMD monolayers studied exhibit $\sigma_{OH}^x = \sigma_{OH}^y = 0$. In column 6 we show that the spin Hall conductivities $|\sigma_{SH}|$ also vanish, as expected. The band gaps E_g are displayed in column 7. The calculated topological invariants $[K_1^{(3)}]$ and $[K_2^{(3)}]$, and the charge of the corner states $Q_c^{(3)}$, all defined in the main text, are given in columns 8, 9 and 10, respectively.

Fig. S5 shows the electronic energy bands calculated with the PAO Hamiltonian along some high symmetry directions of the two-dimensional (2D) BZ. The color-code indicates the expectation value of the \hat{z} -component of the OAM operator given by

$$\ell_{z,n}(\mathbf{k}) = \langle u_{n,\mathbf{k}} | \hat{L}_z | u_{n,\mathbf{k}} \rangle. \quad (\text{S6})$$

In our color convention, the blue (red) tonalities represents an OAM polarization that approaches $2\hbar$ ($-2\hbar$), indicating dominance of the transition-metal atoms' d-shell. We shifted the energy scale to make the origin coincide with the Fermi-level.

In Fig. S6, we depict the orbital-weighted Berry curvatures of the valence-bands, defined by Eq. (S4), calculated for all the 2H TMD monolayers listed in the table II, along some high-symmetry directions of the 2D BZ.

Discussion We notice two qualitatively distinct behaviors in the results depicted in Figs. S5 and S6. Mo-, Cr- and W-based systems exhibit a direct energy band gap and the top of the valence-band occurs at K valleys, where the eigenstates have strong d -character and are highly polarized along the out-of-plane \hat{z} -direction, indicated by the intense blue tonality of the energy band spectra in this energy region. The expectation values of the \hat{z} component of the OAM calculated at the top of the valence bands ($\ell_z(K)$) are quoted in the right upper corners of the Fig. S5 panels. For M=Mo, Cr and W, the orbital-weighted Berry curvatures are strongly peaked around the K-valleys. This means that the physics of OAM can be well described by a Dirac model¹⁹ whose valence-band involves the linear combinations of transition metal d states ($|d_{x^2-y^2} - i\tau d_{xy}\rangle/\sqrt{2}$) which carry OAM $2\tau\hbar$, where $\tau = \pm 1$ for K and K' valleys. However, for Ti, the transition-metals d-shell-band is positioned above the electronic band-gap, i.e., in the conduction band. On the other hand, the gap is indirect, and $\Omega^{L_z}(\mathbf{k})$ is more spread throughout the BZ. Consequently, the OHC plateau in the insulating gap $|\sigma_{OH}|$ for H-TMDs of Ti is always smaller than $1.0 \times (e/2\pi)$ [see table II].

IV. 1T-TMDS

Table III extends the Table II presented in the main text. It includes all insulating TMD monolayers that naturally stabilize in the 1T structural phase. They are listed here in decreasing order of their orbital Hall conductivity plateaus.

Discussion TMD monolayers in the 1T structural phase are centrosymmetric. As a result, the band-structure is spin degenerate and the expectation value $\langle \ell_z \rangle_{n,\mathbf{k}} = 0$ for the spin degenerate bands.

Fig. S7 shows the electronic energy bands calculated along some high-symmetry directions of the 2D BZ, and the orbital Hall conductivities σ_{OH}^x , σ_{OH}^y and σ_{OH}^z , calculated as functions of energy, for all 1T TMD monolayers listed in table III. Differently from the 2H structures, most 1T TMDs have indirect energy band gaps. Also, the top of

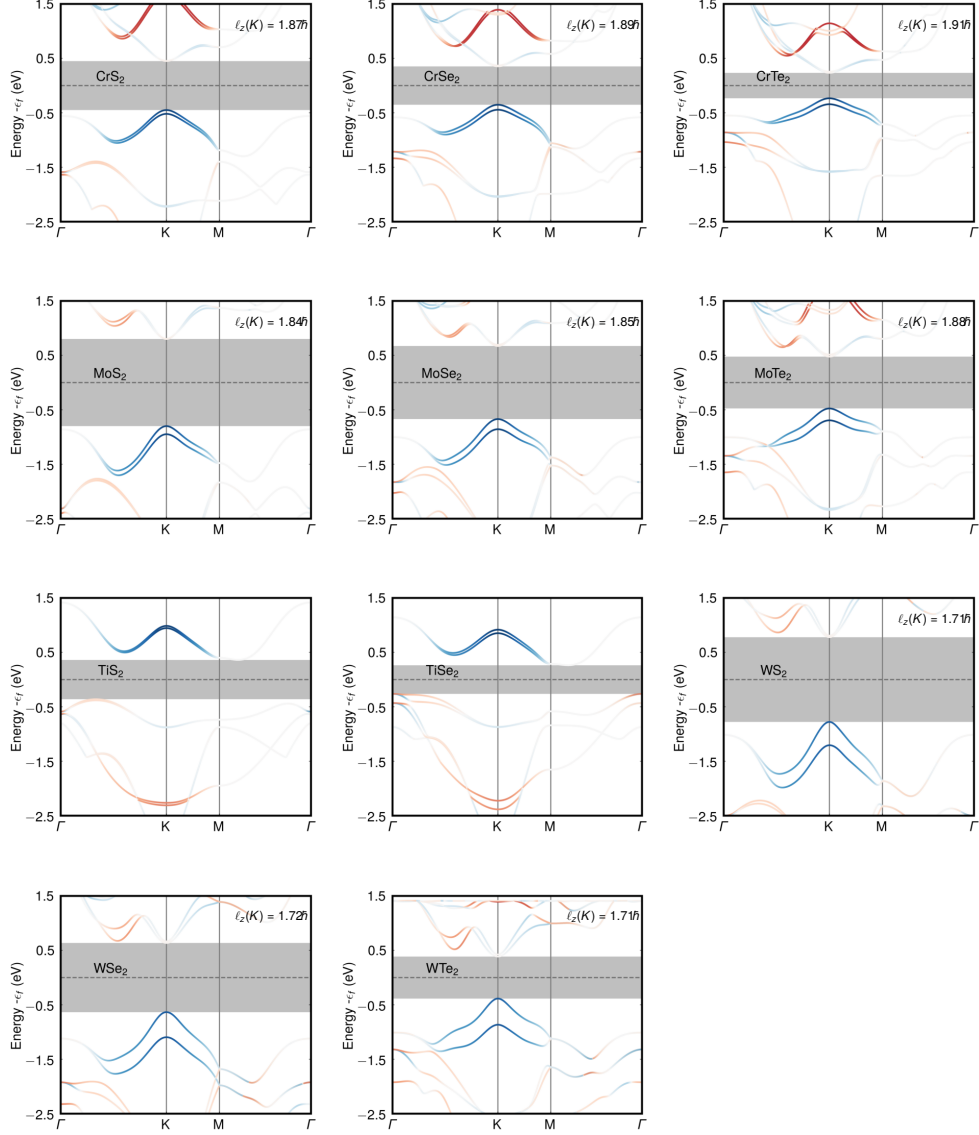


Figure S5: Electronic energy bands of the 2H TMD monolayers listed in table II, calculated with the PAO Hamiltonian along some high-symmetry directions of the 2D BZ. The color code illustrates the corresponding expectation values of ℓ_z . For compounds that display direct energy band gap centered at the K and K' symmetry points, we explicitly quote the value of $\ell_z(K)$ in the figure. The blue (red) tonalities indicates a polarization of OAM that approaches $2\hbar$ ($-2\hbar$).

the valence bands have contribution of different sets of states that can behave as pseudo-spinors. This results in orbital-weighted Berry curvatures that have two different components and are spread over the whole Brillouin zone.

The orbital Hall conductivity also has two different components, although L_z is still the main contribution to the orbital Hall effect in the insulating phase.

V. CONNECTION BETWEEN HIGHER ORDER TOPOLOGICAL INSULATORS AND ORBITAL HALL EFFECT IN A LOW ENERGY MODEL

To show a direct connection between HOTIs and the orbital Hall effect, let us consider the effective model presented in Ref. 45 to characterize the higher-order topological phase of Bismuth. In that case, the topology of Bismuth is

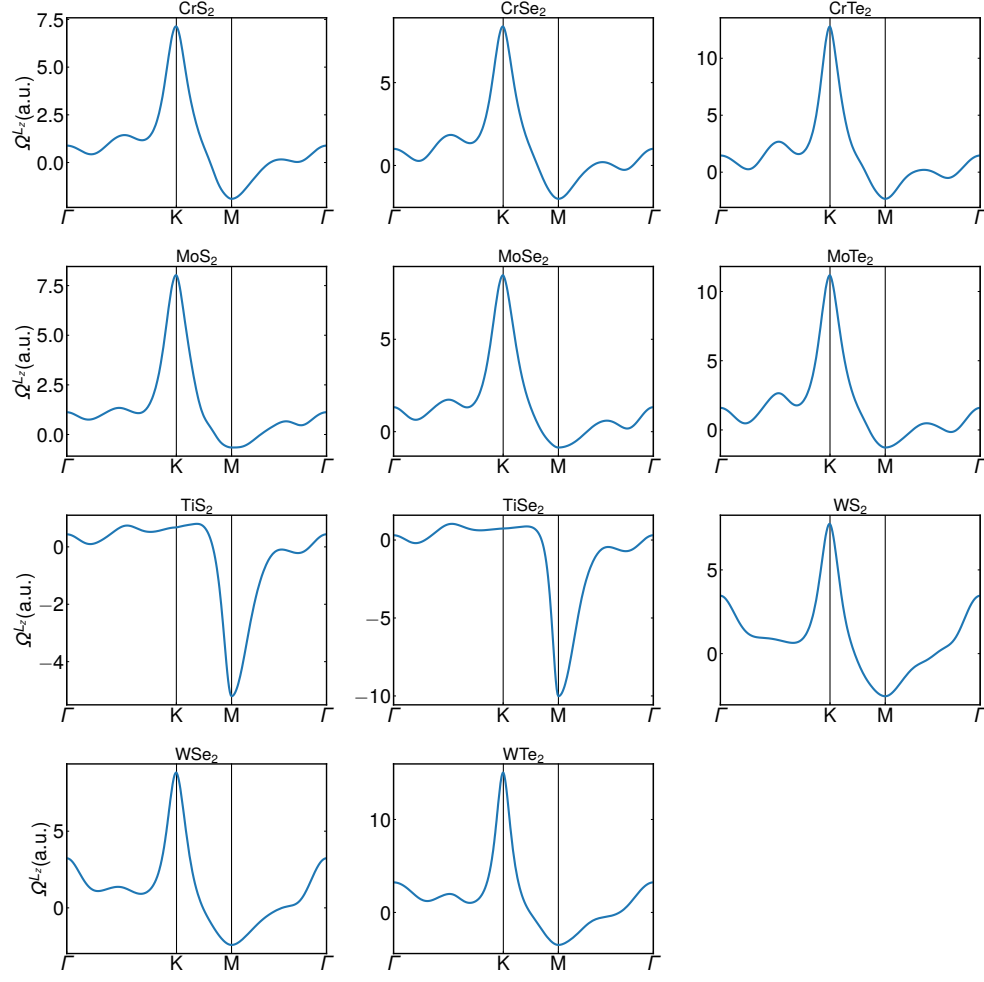


Figure S6: Orbital-weighted Berry curvatures of the valence-bands, defined by Eq. (S4), calculated for all the 2H TMD monolayers listed in Table II, along some high-symmetry directions in the 2D BZ .

protected by the combination of the \hat{C}_3 rotation, \mathcal{I} and \mathcal{T} symmetries, and the authors demonstrated that the existence of multiple band inversions occurring within subspaces characterized by their rotation eigenvalues is overlooked by the first-topological index proposed by Fu and Kane⁸¹. Similarly to Bismuth, the two classes of TMDs discussed here (1T and 1H) also present two band inversions. To construct an effective low-energy model for Bismuth, the authors used a Dirac model representation of a HOTI based on the Bernevig-Hughes-Zhang (BHZ) model for topological insulators. It consists of two diagonal blocks containing two BHZ-like models that respect \hat{C}_3 rotation symmetry and \mathcal{I} .

Individually, they have a single band inversion and are topological insulators. When connected, they present two band inversions and are indexed as HOTI. Let us start exploring the characteristics of a single BHZ Hamiltonian. Following the supplementary material of Ref. 45, if one considers the basis $\{|p_+ \uparrow\rangle, |d_+ \downarrow\rangle, |p_- \downarrow\rangle, |d_- \uparrow\rangle\}$ where $p_{\pm} = p_x \pm ip_y$ and $d_{\pm} = d_{xy} \pm id_{x^2-y^2}$, the BHZ model can be written as:

$$\mathcal{H}_T(\mathbf{k}) = \begin{bmatrix} \mathcal{H}(\mathbf{k}) & 0 \\ 0 & \mathcal{H}^*(-\mathbf{k}) \end{bmatrix} \quad (\text{S7})$$

where

$$\mathcal{H}(\mathbf{k}) = \begin{bmatrix} M(k) & v_f k_+ \\ v_f K_- & -M(k) \end{bmatrix}, \quad (\text{S8})$$

1T-TMD (Z_M)	σ_{OH}^x	σ_{OH}^y	σ_{OH}^z	$ \sigma_{OH} $	$ \sigma_{SH} $	$E_g(\text{eV})$	\mathbb{Z}_4
NiS ₂ (28)	0	1.02	-1.78	2.05	0.00	0.54	2
PdS ₂ (46)	0	0.73	-1.22	1.42	0.00	1.14	2
PdSe ₂ (46)	0	0.85	-1.65	1.85	0.00	0.52	2
PtTe ₂ (78)	0	0.82	-1.59	1.70	0.00	0.37	2
PtSe ₂ (78)	0	0.60	-1.01	1.18	0.00	1.17	2
PtS ₂ (78)	0	0.51	-0.77	0.92	0.00	1.72	2
ZrS ₂ (40)	0	0.61	-0.34	0.70	0.00	1.16	2
ZrSe ₂ (40)	0	0.84	-0.58	1.02	0.00	0.34	2
HfS ₂ (72)	0	0.32	-0.08	0.33	0.00	1.27	2
HfSe ₂ (72)	0	0.71	-0.40	1.02	0.00	0.48	2
NiO ₂ (28)	0	0.51	-0.76	0.91	0.00	1.25	2
PdO ₂ (46)	0	0.37	-0.46	0.59	0.00	1.39	2
PtO ₂ (78)	0	0.26	-0.27	0.37	0.00	1.70	2

Table III: Orbital Hall conductivity of TMD monolayers in the 1T structural phase. In the first column, we list the compound and the atomic number of its transition metal atom (Z_M). Columns 2-5 show the corresponding OHCs within their insulating gaps (σ_{OH}^η , for $\eta = x, y, z$, and $|\sigma_{OH}|$), respectively. All the OHCs are given in units of $e/2\pi$. In column 6 we show that the spin Hall conductivities $|\sigma_{SH}|$ vanish, as expected. The band gaps E_g are displayed in column 7, and column 8 shows that the topological indicator $\mathbb{Z}_4 = 2$, for all elements in this table.

where $k^2 = k_x^2 + k_y^2$, $k_\pm = k_x \pm ik_y$. The effective mass $M(\mathbf{k})$ is given by $M(\mathbf{k}) = B - Mk^2$, where B and M are two real constants. The transition between the topological and trivial insulating phases occurs when M changes sign.

The Berry curvature of the valence band of each block is given by

$$\Omega^s(k) = s \frac{v_f^2(M + Bk^2)}{((M - Bk^2)^2 + v_f^2 k^2)^{3/2}}$$

where $s = \pm$ is the block index, v_f represents the Fermi velocity, and

The $s = \pm$ contributions of each block to the total Berry curvature are depicted in the left panel of figure S9. They exhibit an extremum at $k=0$, where the band inversion occurs, and tend to zero as $\sim \pm 1/k$ for large values of k . We note that even for $B = 0$, the system is a \mathbb{Z}_2 topological insulator, and the total Berry curvature for this model is zero, as expected for time-reversal symmetric systems. In contrast, the $s = \pm$ contributions from each block to the orbital-weighted Berry curvature are identical and given by

$$\Omega^L(k) = \frac{3\hbar}{4} \frac{v_f^2(M + Bk^2)}{((M - Bk^2)^2 + v_f^2 k^2)^{3/2}}.$$

They are portrayed in the right panel of figure S9 and clearly lead to a non-null total orbital Berry curvature, whose $\sim 1/k$ decay for large k implies that the BHZ model describes a \mathbb{Z}_2 topological insulator with a sizable orbital Hall effect.

The Dirac representation of a HOTI with $\mathcal{T}, \hat{\mathcal{C}}_3$ and \mathcal{I} symmetries in the basis of orbitals $\{|p_- \uparrow\rangle, |d_- \downarrow\rangle, |p_+ \downarrow\rangle, |d_+ \uparrow\rangle, |p_+ \uparrow\rangle, |d_+ \downarrow\rangle, |p_- \downarrow\rangle, |d_- \uparrow\rangle\}$ can be expressed as

$$H(\mathbf{k}) = H_1(\mathbf{k}) \oplus H_3(\mathbf{k}), \quad (\text{S9})$$

where $H_1(\mathbf{k})$ and $H_3(\mathbf{k})$ are disconnected blocks of the Hamiltonian characterized by the rotation eigenvalues -1 and $e^{\pm i\pi/3}$, respectively. Each block is defined by

$$H_j(\mathbf{k}) = \begin{pmatrix} M(\mathbf{k}) & v_f k_+^j & 0 & 0 \\ v_f k_-^j & -M(\mathbf{k}) & 0 & 0 \\ 0 & 0 & M(\mathbf{k}) & -v_f k_-^j \\ 0 & 0 & -v_f k_+^j & -M(\mathbf{k}) \end{pmatrix}, \quad (\text{S10})$$

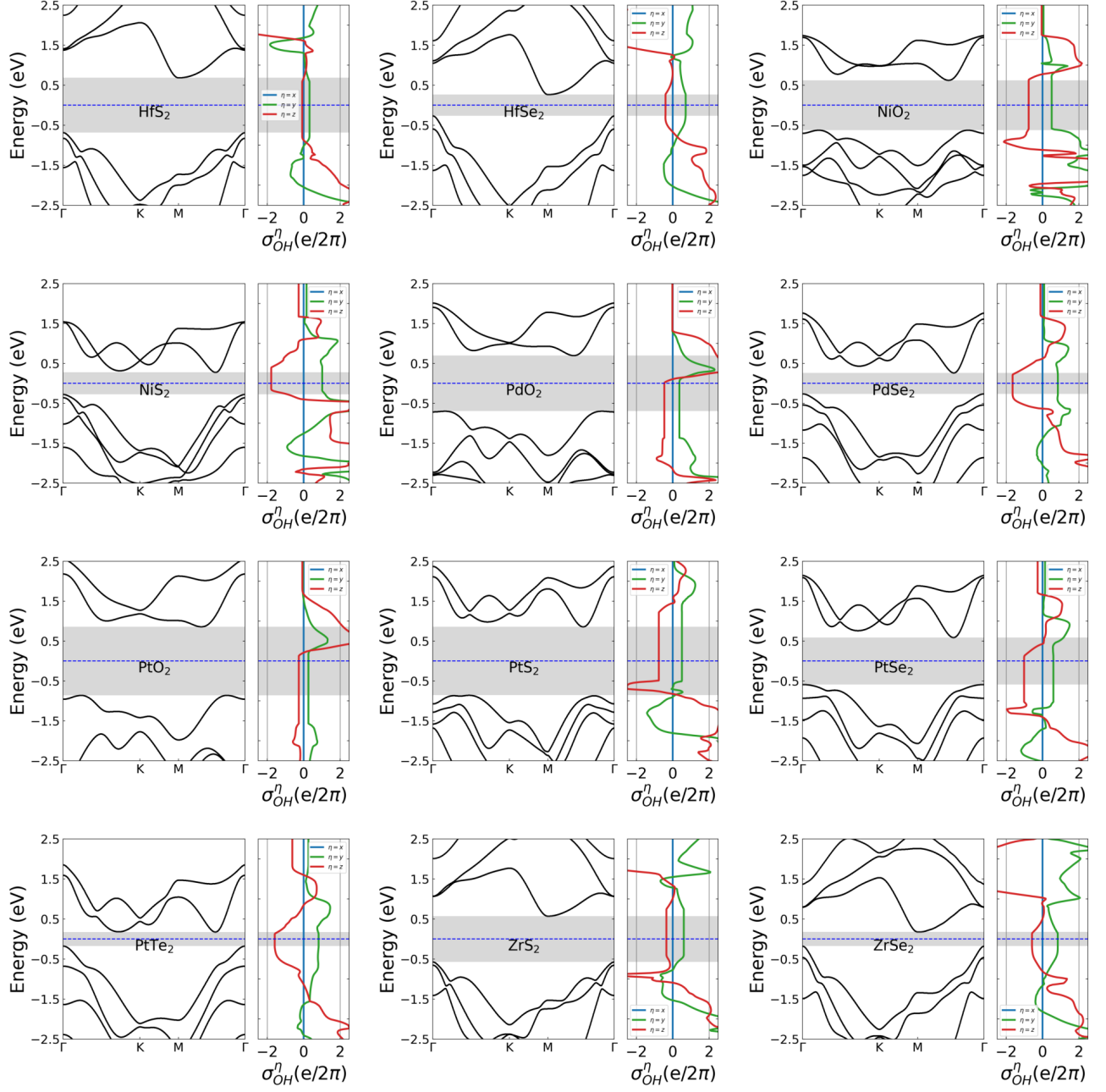


Figure S7: Electronic energy bands calculated along some high-symmetry directions of the 2D BZ are exhibited in the left panels for all 1T TMD monolayers listed in Table III. The corresponding orbital Hall conductivities σ_{OH}^x , σ_{OH}^y and σ_{OH}^z , calculated as functions of energy, are depicted by the green, blue and red lines, respectively, in the right panels.

for $j = 1, 3$. Here $k_{\pm} = k_x \pm ik_y$, $k_{\pm}^j = (k_{\pm})^j$. We note that $H_1(\mathbf{k})$ represents the BHZ model given by Eq. S7. The off-diagonal terms in each $H_3(\mathbf{k})$ block are altered to k_{\pm}^3 in order to comply with \mathcal{T} and the corresponding representation of \hat{C}_3 . Nevertheless, $H_3(\mathbf{k})$ also describes a \mathbb{Z}_2 TI.

The Berry curvature of the valence band associated with each sub-block of $H_3(\mathbf{k})$ is given (in polar coordinates) by

$$\Omega^s(k) = s \frac{3}{4} \frac{k^4(3M - Bk^2)}{((M - Bk^2)^2 + v_f^2 k^6)^{3/2}}$$

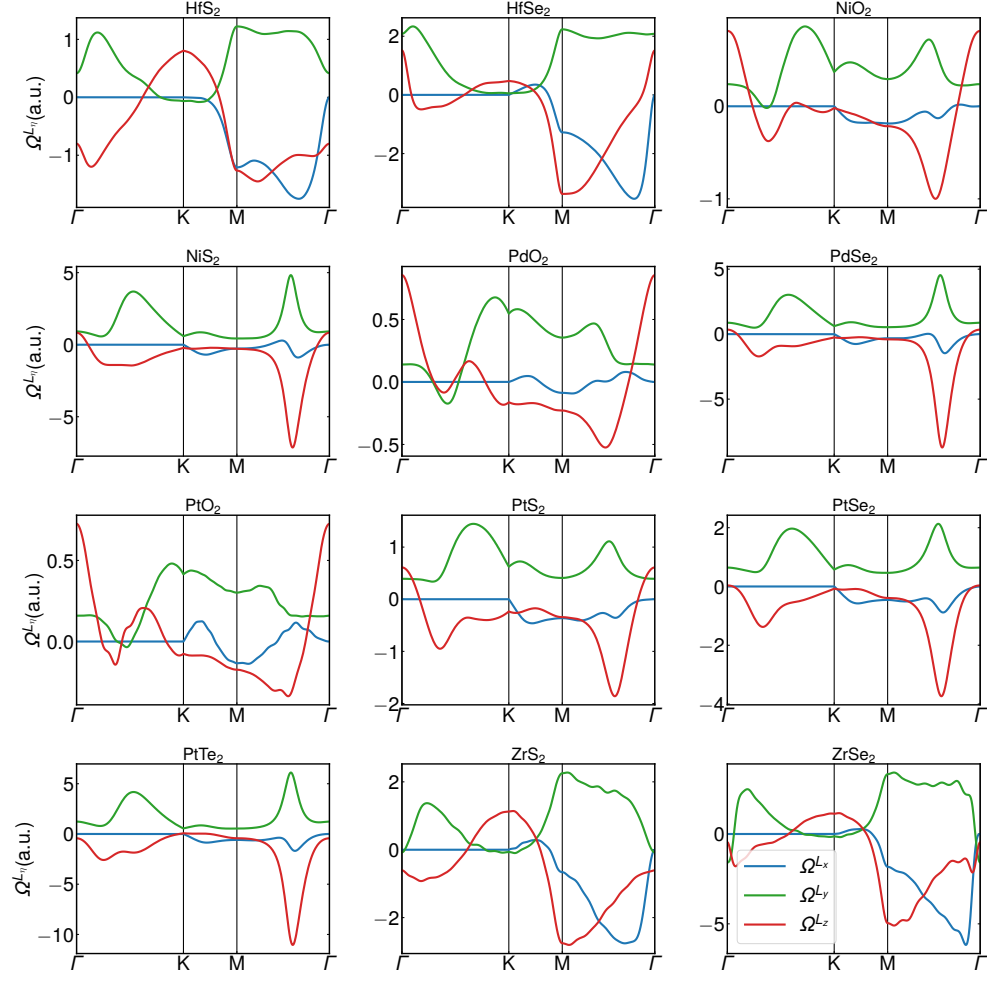


Figure S8: For each 1T monolayer TMD presented in the table, we show the orbital-weighted Berry-curvature of the valence-band for the three components of the OAM.

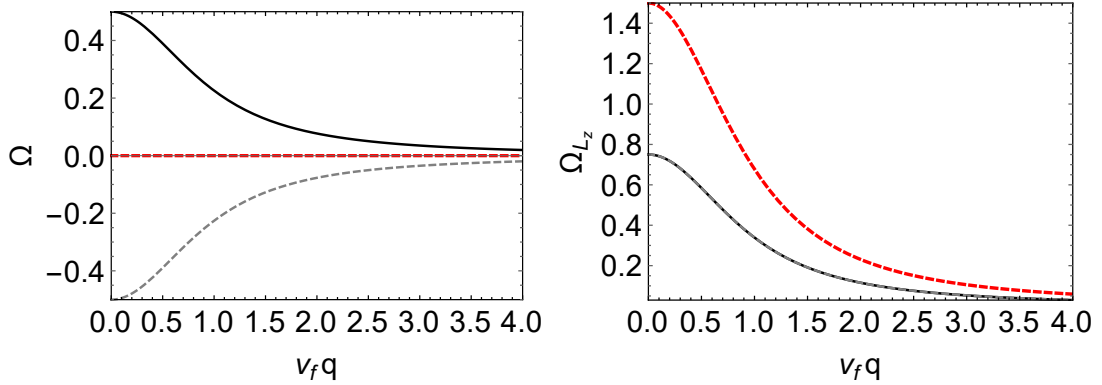


Figure S9: Berry (left panel) and orbital-weighted Berry curvatures (right panel) calculated for the BHZ model with $M = 1$ and $B = 0.1$. The black solid and grey dashed lines represent the contributions from the $s = +$ and $s = -$ blocks, respectively. Note that the two contributions are identical in panel (b). The red dashed lines depict the sum of the $s = \pm$ contributions that define the corresponding Berry and orbital-weighted Berry curvatures.

where $s = \pm$ is the sub-block index.

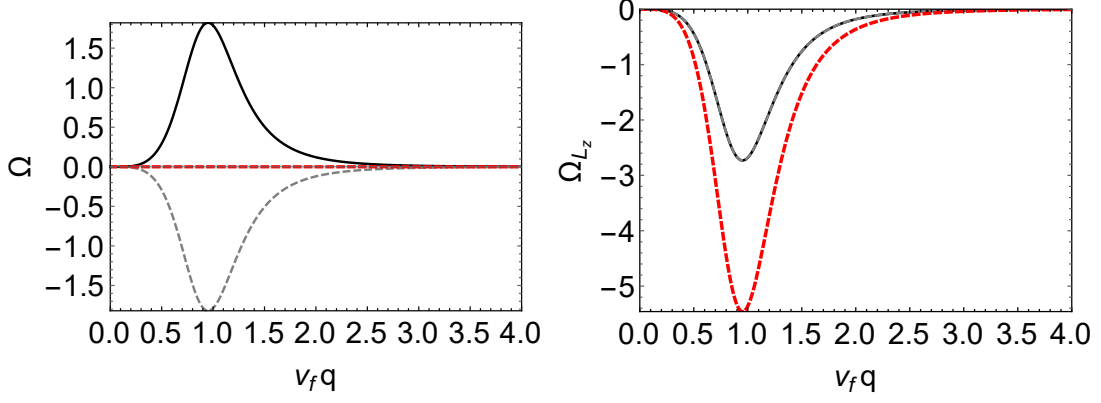


Figure S10: Berry (left panel) and orbital-weighted Berry curvatures (right panel) calculated for the H_3 model with $M = 1$ and $B = 0.1$. The black solid and grey dashed lines correspond to the contributions from the $s = +$ and $s = -$ blocks, respectively. The red dashed lines depict the total Berry and orbital-weighted Berry curvatures, which are given by the corresponding sums of the $s = +$ and $s = -$ contributions.

In the left panel of figure S10, we note that due to the modification of the off-diagonal terms in $H_3(\mathbf{k})$ the extrema of $s = \pm$ contributions to the Berry curvature are located at $k \neq 0$, and for large values of k they decay as $\sim \pm 1/k^3$. Similarly to $H_1(\mathbf{k})$, even for $B = 0$, the system is a \mathbb{Z}_2 topological insulator, and the total Berry curvature for the model vanishes, as expected for time-reversal symmetric systems. However, the $s = \pm$ contributions to the orbital-weighted Berry curvature are identical and given by

$$\Omega^L(k) = -\frac{9\hbar}{4} \frac{v_f^2 k^4 (M - Bk^2)}{((M - Bk^2)^2 + v_f^2 k^6)^{3/2}}.$$

The right panel of figure S10 depicts the $s = \pm$ contributions and the total orbital-weighted Berry curvature for the $H_3(\mathbf{k})$ model. The non-vanishing total orbital Berry curvature and its $1/k^3$ decay for large k imply that it also describes a \mathbb{Z}_2 topological insulator with a sizable orbital Hall effect. Since $H_1(\mathbf{k})$ and $H_3(\mathbf{k})$ present a band inversion, the complete Hamiltonian represents a HOTI⁴⁵ with finite orbital Hall effect as the total orbital Berry curvature remains sizable. This explicitly shows that any HOTI that is reasonably described by the model Hamiltonian given by Eqs. S9 and S10 will exhibit finite orbital Hall conductivity.

VI. CONNECTION BETWEEN HIGHER-ORDER TOPOLOGICAL INSULATORS AND ORBITAL HALL EFFECT IN A MULTI-ORBITAL TRIANGULAR LATTICE FOR 2H-TMDs

Here, we follow a recipe to obtain an electronic 2D HOTI on a multiorbital triangular lattice, as presented in reference 64. One key aspect of this approach is the possibility of tuning the appearance of different topological phases by changing a few parameters. In this work, Eck *et al.* demonstrated that the essential ingredients for the emergence of the HOTI phase are the spin-orbit coupling and two terms that break the inversion and the horizontal mirror symmetries. Surprisingly, the three-band model commonly used to describe the low-energy electronic properties of 2H TMDs falls within the same class of triangular lattice systems. To illustrate this, we will focus on the competition between the spin-orbit coupling and terms that break the inversion symmetry of the Hamiltonian. Using the basis $\{d_{z^2}, d_{xy}, d_{x^2-y^2}\}$, the three bands model can be written as

$$H = \begin{bmatrix} h_0 & h_1 & h_2 \\ h_1^* & h_{11} & h_{12} \\ h_2^* & h_{12}^* & h_{22} \end{bmatrix}, \quad (\text{S11})$$

where

$$h_0 = 2t_0(\cos 2\alpha + 2 \cos \alpha \cos \beta) + \epsilon_1, \quad (\text{S12})$$

$$h_1 = -2\sqrt{3}t_2 \sin \alpha \sin \beta + 2it_1(\sin 2\alpha + \sin \alpha \cos \beta) \quad (\text{S13})$$

$$h_2 = 2t_2(\cos 2\alpha - \cos \alpha \cos \beta) + 2\sqrt{3}it_1 \cos \alpha \sin \beta, \quad (\text{S14})$$

$$h_{11} = 2t_{11} \cos 2\alpha + (t_{11} + 3t_{22}) \cos \alpha \cos \beta + \epsilon_2, \quad (\text{S15})$$

$$h_{22} = 2t_{22} \cos 2\alpha + (3t_{11} + t_{22}) \cos \alpha \cos \beta + \epsilon_2, \quad (\text{S16})$$

$$h_{12} = \sqrt{3}(t_{22} - t_{11}) \sin \alpha \sin \beta + 4it_{12} \sin \alpha (\cos \alpha - \cos \beta) \quad (\text{S17})$$

$$\alpha = \frac{1}{2}k_x a \text{ and } \beta = \frac{\sqrt{3}}{2}k_y a. \quad (\text{S18})$$

The spin-orbit coupling can be written as

$$H_{\text{SOC}} = s_z \frac{\lambda}{2} \begin{bmatrix} 0 & 0 & 0 \\ 0 & 0 & 2i \\ 0 & -2i & 0 \end{bmatrix}, \quad (\text{S19})$$

where λ is the strength of the coupling and $s_z = \pm 1/2$ are the eigenstates of the z component of the spin operator.

From equation (S11), we identify that the terms proportional to t_1 , t_2 , and t_{12} are responsible for the inversion symmetry breaking of the system. To illustrate the transition from a HOTI with sizable orbital Hall conductivity to a trivial insulating phase, we will consider the tight-binding parameters of MoS₂ as described in Ref. 46 but increasing the SOC to $\lambda_{\text{SOC}} = 15 \times \lambda_{\text{MoS}_2}$. We focus on two situations. In the first case, we consider the system to have broken inversion symmetry, whereas in the second case, we restore the inversion symmetry of the system and neglect the hybridizations between orbitals in different irreducible representations by setting $t_1 = t_2 = t_{12} = 0$.

Figure S11 shows the bandstructures of the bulk systems and the bandstructures of nanoribbons extracted from them, whereas figure S12 presents the orbital Hall conductivity for the two cases. In the first case (A), we found a strong splitting of the conduction band due to the increased SOC strength. However, the number of edge states within the energy gap separating the valence and conduction bands remains finite. Additionally, it is noticeable that these states do not connect the conduction and valence bands, as in the case of MoS₂. We can see that the orbital Hall conductivity plateau has a height comparable to the one for MoS₂ with weak SOC and the spin Hall conductivity goes to zero within the energy gap confirming that despite the increment in λ_{SOC} the system remains within the orbital Hall insulating phase. If we turn off the couplings that break inversion symmetry and the couplings that hybridize different irreducible representations ($t_1 = t_2 = t_{12} = 0$), we can see that in the second case (B) the strong SOC is responsible for opening a band gap. However, different from the previous case, the bandstructure of its nanoribbon does not have in-gap edge states, and the system is a trivial insulator with vanishing orbital Hall conductivity.

The different orbital properties in the two cases previously discussed can be understood in terms of the orbital hybridizations in the system. In the first case, the presence of t_1, t_2 and t_{12} not only breaks the inversion symmetry but allows the hybridization between the d_{z^2} orbitals and the orbitals d_{xy} and $d_{x^2-y^2}$, whose superposition can carry non-zero orbital angular momentum. Thus allowing the appearance of orbital textures on reciprocal space and leading to the sizable orbital Berry curvature manifested in the SOC-independent orbital Hall conductivity plateau displayed in figure S12. Nonetheless, in the second case, the opposite occurs. Restoring the inversion symmetry also increases the rotational symmetry of the system, which changes the point group symmetry of the system from D_{3h} to D_{6h} as a consequence of inhibiting hybridizations between the orbitals of the system. Thus there are no orbital angular momentum textures and the formation of orbital pseudospinors in the system is heavily reduced, and now it is a trivial insulator dominated by the SOC. Our analysis and the appearance of a HOTI phase when lattice symmetries are broken and produce band inversions are consistent with the results from Ref. 64.

VII. ORBITAL CHARACTER OF PTS₂ BANDS

As mentioned in the main text, the D_{3d} symmetry of the 1T transition metal dichalcogenides imposes that the p orbitals of the sulfur atoms will significantly contribute to upper valence energy bands near Γ . Figure S13 portrays

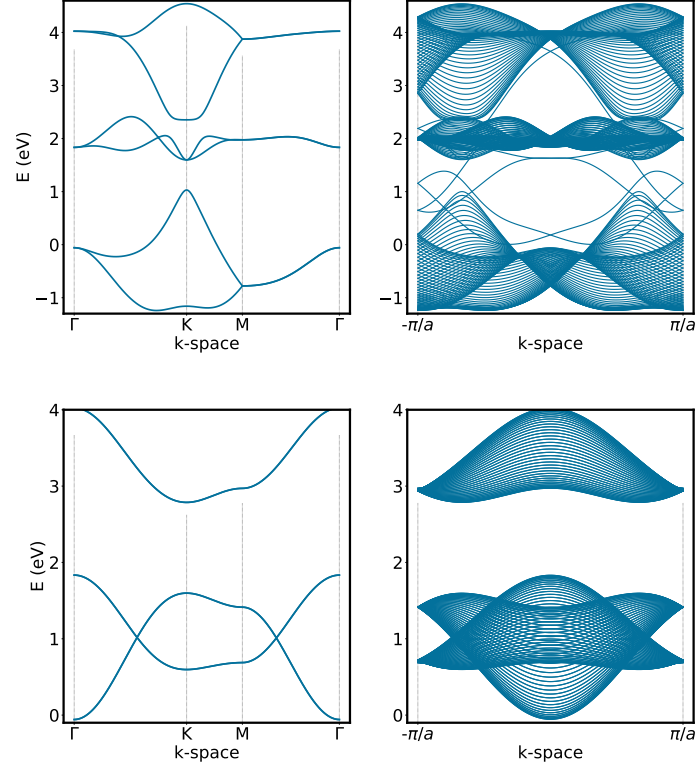


Figure S11: Upper panel: bulk (left) and nanoribbon (right) band structures for the three bands model of MoS₂ with strong SOC (case A). Lower panel: bulk (left) and nanoribbon (right) band structures for the three bands model of MoS₂ with strong SOC and $t_1 = t_2 = t_{12} = 0$ (case B).

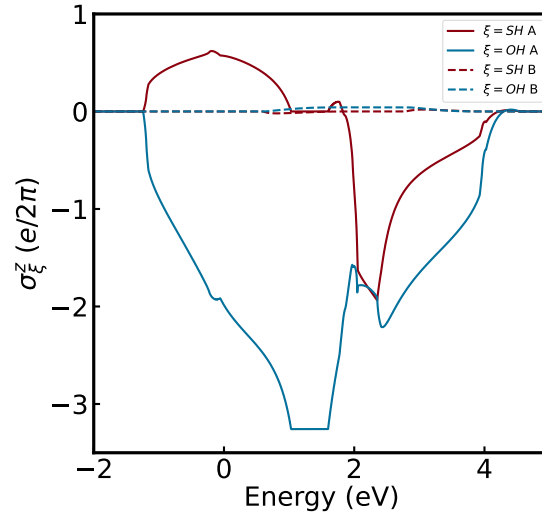


Figure S12: Orbital Hall conductivity (blue line) and spin Hall conductivity (red) for the three bands model of MoS₂ with strong SOC (case A - solid) and for the three bands model of MoS₂ with strong SOC and $t_1 = t_2 = t_{12} = 0$ (case B - dashed line).

the orbital projections of the energy bands for PtSe₂. Panel (a) shows the contribution to the energy states from the p orbitals of the sulfur atoms, and panel (b) corresponds to the d orbitals of the transition metal. From the orbital projections highlighted in panel (a), it is clear that the p_x and p_y orbitals have the dominant contribution to the energy states of the conduction band around Γ . This state arrangement occurs due to the local asymmetry experienced by

the sulfurs on each atomic plane, as we mentioned in the main text. However, as panel (b) portrays, afar from Γ , the dominant character for the energy states will be given by the p_z orbitals and the pseudospinors formed by the linear combinations of the d_{xz} , d_{yz} , d_{xy} , and $d_{x^2-y^2}$ orbitals from the platinum. In particular, they will dominate around the K and M points, and their contributions can be related to the existence of non-vanishing $\sigma_{OH}^{L_x}$ and $\sigma_{OH}^{L_y}$ responses as reported in table III.

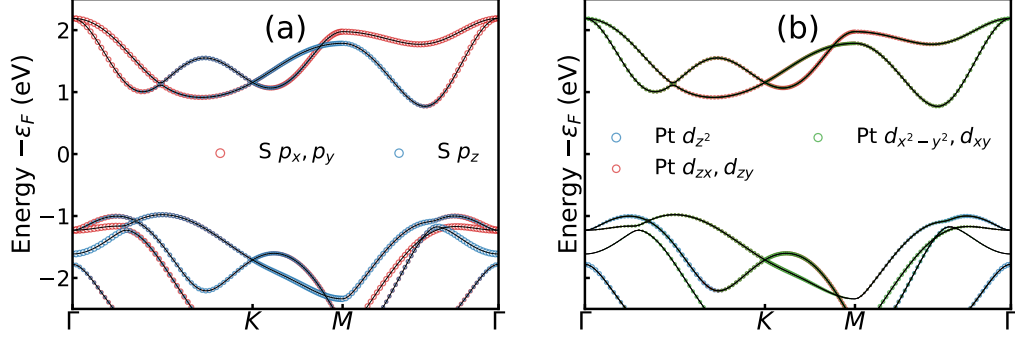


Figure S13: Orbital projection of the bulk energy bands of PtS₂. (a) Contribution from the p_x, p_y (red circles) and p_z (blue circles) orbitals of the Sulfur atoms. (b) Contribution from the d_{z^2} (blue circles), d_{xz}, d_{yz} (red circles) and $d_{xy}, d_{x^2-y^2}$ (green circles) orbitals of the Platinum atoms.

VIII. RELATION BETWEEN PSEUDO-TIME-REVERSAL AND THE L_z OPERATOR FOR 2H TMDs

Before showing the relationship between the operator for the calculation of the orbital Chern number and the pseudo-time-reversal operator, let us write the latter. Since the d_z orbitals belong to a 1×1 irreducible representation (A'_1), they will transform as a scalar under the pseudo-time-reversal symmetry. However, following the procedure used in reference⁸², we can use the rotation operators to determine the pseudo-time-reversal operations of the states d_{xy} and $d_{x^2-y^2}$, which belong to the irreducible representation E' of the group D_{3h} . In the $\{|d_{z^2}\rangle, |d_{xy}\rangle, |d_{x^2-y^2}\rangle\}$ basis, the rotation operators for the 1H TMDs reads:

$$R_z\left(\frac{2\pi}{3}\right) = \begin{pmatrix} 1 & 0 & 0 \\ 0 & -\frac{1}{2} & \frac{\sqrt{3}}{2} \\ 0 & -\frac{\sqrt{3}}{2} & -\frac{1}{2} \end{pmatrix} \quad R_z\left(-\frac{2\pi}{3}\right) = \begin{pmatrix} 1 & 0 & 0 \\ 0 & -\frac{1}{2} & -\frac{\sqrt{3}}{2} \\ 0 & \frac{\sqrt{3}}{2} & -\frac{1}{2} \end{pmatrix} \quad (\text{S20})$$

where the operator $R_z(\phi)$ represents a rotation operator of angle ϕ around the \hat{z} -axis. The rotation operators are block-diagonal, evincing that the d_{z^2} , and the orbitals d_{xy} and $d_{x^2-y^2}$ belong to different irreducible representations. Moreover, the difference between the two rotation operators defined in Eq. S20 is restricted to the 2×2 subspace spanned by the orbitals d_{xy} and $d_{x^2-y^2}$, which may combine, to form a pair of pseudo-spins. Therefore for this subspace, we may define the pseudo-time-reversal operator $\mathcal{T}_p = UK$, where the operator \mathcal{K} represents the complex conjugation operator, and U represents the unitary part of the pseudo-time-reversal symmetry operator given by:

$$U = \frac{1}{\sqrt{3}} \left(R_z\left(\frac{2\pi}{3}\right) - R_z\left(-\frac{2\pi}{3}\right) \right) = i\sigma_y \quad (\text{S21})$$

where σ_y is the usual Pauli matrix acting in the pseudo-spins' subspace.

Now that we have defined the pseudo-time-reversal operator, one can verify that when applied to valence band states $|\psi_\tau\rangle = (|d_{x^2-y^2}^1\rangle - i\tau|d_{xy}^1\rangle)/\sqrt{2}$ at the K point, it translates them to the other valley, similarly to the time-reversal operator. As far as the connection between the pseudo-time-reversal and orbital angular momentum operator is concerned, we may expand U given by Eq. S21 in powers of L_z to show that it is proportional to L_z . Hence, one can redefine the operator used in the orbital Chern number calculation presented in reference¹⁹ as the difference between the rotation operator and its time-reversed partner.

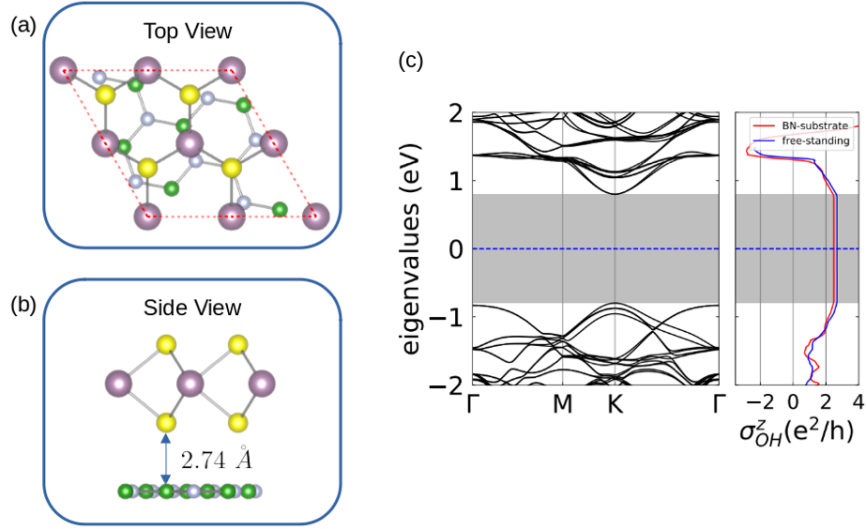
IX. EFFECT OF *h*-BN SUBSTRATE

Figure S14: Top view (a) and side view (b) of MoS₂ on hBN substrate. (c) Band structure and orbital Hall conductivity of the MoS₂-hBN bilayer.

To study the effect of substrate usually present in typical experiments on orbital transport, we performed DFT calculations for a single layer of H-MoS₂ on top of a hexagonal boron nitride layer (hBN). Due to the lattice mismatch, $a_{\text{MoS}_2} = 3.18 \text{ \AA}$ and $a_{\text{hBN}} = 2.51 \text{ \AA}$, we constructed a supercell with a MoS₂ 2x2 and an hBN $\sqrt{7} \times \sqrt{7}$ to reduce the mismatch. As a result, our lattice mismatch is smaller than 5%. We preserved the MoS₂ structure and strained the hBN substrate (we also did the opposite and obtained similar results, with a small change in the band gap). The top and side views of the structure are shown in Fig. S14, panels (a) and (b), respectively. To correctly describe the dispersion forces between the two materials we included a Van Der Waals correction, resulting in a 2.74 Å interlayer distance. In Fig. S14 (c) we show its band structure along with the OHC (red line). The OHC for the free-standing H-MoS₂ monolayer (represented by the blue line) is included for comparison. We note that the OHC inside the insulating gap is practically unaffected by the substrate.